FULL PAPER

Magnetic Resonance in Medicine 00:00–00 (2015)

A Theoretical Approach Based on Electromagnetic Scattering for Analysing Dielectric Shimming in High-Field MRI

Wyger M. Brink,[1] Rob F. Remis,[2] and Andrew G. Webb[1]*

Purpose: In this study, we analyzed dielectric shimming by formulating it as an electromagnetic scattering problem using integral equations.

Methods: Three-dimensional simulations of the radiofrequency field in two configurations using different materials were analyzed in terms of induced currents and secondary fields. A two-dimensional integral equation method with different backgrounds was used to identify the underlying physical mechanisms. This framework was then used to develop an inversion method for the design of dielectric pads.

Results: The effects of a dielectric pad can be attributed to the interference of a secondary field that is produced by the currents induced in the dielectric pad, radiating in an inhomogeneous background. The integral equation method with inhomogeneous background reduces the complexity of the forward and inverse problem significantly and can be used to optimize the permittivity distribution for a desired B_1^+ field. Agreement with experimental B_1^+ maps was obtained in a cylindrical phantom, demonstrating the validity of the method.

Conclusions: The integral equation method with inhomogeneous background yields an efficient numerical framework for the analysis and inverse design of dielectric shimming materials. **Magn Reson Med 000:000–000, 2015. © 2015 Wiley Periodicals, Inc.**

Key words: Dielectric shimming; B_1^+; electromagnetic scattering; integral equations; inverse problem

INTRODUCTION

The use of high permittivity ($\varepsilon_r > 100$) dielectric materials has been shown to be an effective method for addressing transmit (B_1^+) inhomogeneities in various applications of high-field MRI, such as body imaging at 3T (1–5) and neuroimaging at 7T (6–9). The term "high-field" here denotes that the dimensions of the body part being imaged are comparable to the radiofrequency (RF) wavelength. The resulting standing wave patterns in the subject decrease the B_1^+ uniformity, leading to spatially variant contrast, or image shading, and a decreased diagnostic value. These patterns can be altered significantly by introducing dielectric materials between the RF coil and the subject, a technique sometimes referred to as "dielectric shimming." Various beneficial effects of this approach have been evaluated in the literature, including an improved B_1^+ homogeneity, reduced specific absorption rate (SAR), and increased receive sensitivity (1–11).

Despite significant efforts to characterize and explain the mechanisms underlying these improvements, the existing literature remains limited to intuitive formulations that can at most guide the operator during judicious placement of a dielectric pad. The most general zero-order formulation is that induced currents are produced in the dielectric material, which act as secondary RF sources, effectively superimposing a secondary RF field on the primary RF field produced without dielectric material (1,3,10,12). This reasoning stems from the time-harmonic form of Ampère's law, given by

$$\nabla \times \boldsymbol{B} = \mu(\boldsymbol{J}_i + \boldsymbol{J}_s), \quad [1]$$

where $\boldsymbol{B}$ is the magnetic flux density, $\mu \approx \mu_0$ is the permeability of tissue, and $\boldsymbol{J}_i$ and $\boldsymbol{J}_s$ represent the induced (passive) and source (active) current densities, respectively. The induced current density, which reflects the presence of a dielectric pad, is given by

$$\boldsymbol{J}_i = (\sigma + j\omega\varepsilon_0\varepsilon_r)\boldsymbol{E}, \quad [2]$$

where σ represents electrical conductivity, j is the imaginary unit, ω represents the angular frequency, ε_0 and ε_r represent the permittivity of free space and relative permittivity of the dielectric pad, respectively, and $\boldsymbol{E}$ represents the electric field strength. This interpretation has supported some empirical observations such as a dielectric pad generally leading to a local increase in B_1^+, which means that the material is best used as close to the region of interest (ROI) as possible, and that higher permittivity materials should be considered at lower fields (2–4,10). Based on such a zero-order formulation, a higher ε_r should always be desirable. However, previous studies have shown that this is not the case, and areas of very low transmit efficiency can result from using very high permittivity materials (8). The underlying reason for this discrepancy is related to electrical interactions, such as wavelength effects within the pad and body, which are not taken into account in a zero-order formulation. Moreover, because the equation is in a differential form, it can at most relate to local quantities (i.e., at the interface of the high permittivity material

[1]C. J. Gorter Center for High Field MRI, Department of Radiology, Leiden University Medical Center, Leiden, Netherlands.

[2]Circuits and Systems Group, Faculty of Electrical Engineering, Mathematics and Computer Science, Delft University of Technology, Delft, Netherlands.

*Correspondence to: Andrew G. Webb, Ph.D., C. J. Gorter Center for High Field MRI, Department of Radiology, Postzone C3-Q, Leiden University Medical Center, Albinusdreef 2, 2333 ZA, Leiden, Netherlands.
E-mail: a.webb@lumc.nl

Received 23 December 2014; revised 15 April 2015; accepted 2 May 2015
DOI 10.1002/mrm.25783
Published online 00 Month 2015 in Wiley Online Library (wileyonlinelibrary.com).

and the body). The description therefore remains limited in terms of providing a *quantitative* prediction of the B_1^+ field within the body. The necessity of a more elaborate understanding of the underlying mechanisms is further emphasized by the continuous increase in high permittivity materials available, some with $\varepsilon_r > 1000$ (13), which produce very strong effects that are likely to exceed the mechanisms described by the zero-order formulation. A better understanding of the underlying mechanisms is therefore required to manage these effects.

Optimizing the design of dielectric pads in terms of their geometry, composition, and placement remains a nontrivial task, because a closed-form solution of their effect has not been demonstrated. The most pragmatic approach so far has been to set up a series of electromagnetic simulations using commercial software for a limited set of configurations, from which the optimal solution is determined a posteriori based on a suitable performance measure (2,3,8,9,14). This procedure can lead to long computation times, especially when multiple degrees of freedom (e.g., dimensions, position, material properties, etc) need to be addressed simultaneously, leading to a large set of configurations that need to be evaluated. In some cases, subject specificity may further increase the complexity of the design problem (9). Some analytical formulations have been proposed that speed up field computation and can be used to analyze fundamental limits (15–20), but they fail to capture these practical design considerations because they do not incorporate a realistic body model. Accurate and efficient modeling methods are therefore highly desirable to improve the design procedure.

There is a vast literature on numerical techniques for the computation of electromagnetic fields in inhomogeneous dielectrics such as the human body. Local methods based on the partial differential form of Maxwell's equations, such as the finite-difference time-domain (FDTD) method, are known for their generality and versatility in many application areas. On the other hand, global methods that start from Maxwell's equations in integro-differential form, such as the integral equation method, offer great flexibility in exploiting certain problem properties by customization of the method (e.g., by reducing the problem to the relevant domain or by incorporating suitable approximations and a priori information). Furthermore, inverse scattering methods from remote sensing based on this formulation may provide a framework for developing a numerical method that can optimize the design of dielectric pads (21–23). Preliminary work based on the integral equation method has been described for modeling the effect of a dielectric pad, by formulating this as an electromagnetic scattering problem in which the body model is used as a background model (24). Some approaches in inverse scattering incorporate a priori knowledge such as a background model to formulate an initial estimate of the pertaining fields, while performing subsequent iterations using the free space Green's function. The background model can also be embedded into the Green's function, thereby directly accounting for its electromagnetic interactions at the cost of a more involved numerical procedure for evaluating the Green's function, since a closed-form solution is not available in case of an inhomogeneous background. Moreover, due to the loss of shift invariance, the operator can no longer be evaluated using the fast Fourier transform, which may reduce the speed of the algorithm. This step, however, reduces the computational domain (i.e., in which the unknown induced currents need to be resolved) to that of the dielectric pad by definition, which reduces the problem complexity.

The first goal of the current study was to explore the physical mechanisms underlying dielectric shimming in terms of secondary fields and displacement currents when using two different high permittivity materials at 7T. These studies were performed using conventional three-dimensional (3D) electromagnetic simulation software. The second goal was to study the relevance of electrical interactions within the pad and within the body by comparing the zero-order approximation with full-wave results using the integral equation method in a two-dimensional (2D) configuration. Finally, this framework was used to develop an optimization method for the design of dielectric pads by solving the corresponding inverse problem. The particular illustrative application is neuroimaging at 7T, but the approach is applicable to all field strengths and configurations.

THEORY

The starting point for the integral equation method is to decompose the relevant components of the total field $\{\boldsymbol{E}, B_1^+\}$ into a primary field $\{\boldsymbol{E}^{\mathrm{b}}, B_1^{+,\mathrm{b}}\}$ and a secondary field $\{\boldsymbol{E}^{\mathrm{sec}}, B_1^{+,\mathrm{sec}}\}$, as follows:

$$\boldsymbol{E}(\boldsymbol{r}) = \boldsymbol{E}^{\mathrm{b}}(\boldsymbol{r}) + \boldsymbol{E}^{\mathrm{sec}}(\boldsymbol{r}) \quad [3]$$

$$B_1^+(\boldsymbol{r}) = B_1^{+,\mathrm{b}}(\boldsymbol{r}) + B_1^{+,\mathrm{sec}}(\boldsymbol{r}). \quad [4]$$

Here, $\boldsymbol{r} = (x, y, z)$ denotes the position vector. This decomposition is schematically illustrated in Figure 1. The primary field is the field produced in the background configuration, which consists of a body model and possibly also a coil model, without any dielectric pads in place. The secondary field represents the field generated in the background configuration by the currents induced within the dielectric pad. We denote the spatial domain that encompasses the dielectric pad by $\mathcal{D}_{\mathrm{p}}$. Using integral equations, one can then write the total electric field $\boldsymbol{E}$ as

$$\boldsymbol{E}(r) = \boldsymbol{E}^{\mathrm{b}}(\boldsymbol{r}) + \int_{\boldsymbol{r}' \in \mathcal{D}_{\mathrm{p}}} \overline{\overline{\boldsymbol{G}}}^{\mathrm{b}}(\boldsymbol{r}, \boldsymbol{r}') \chi_{\mathrm{e}}(\boldsymbol{r}') \boldsymbol{E}(\boldsymbol{r}') \mathrm{d}V, \quad [5]$$

where $\overline{\overline{\boldsymbol{G}}}^{\mathrm{b}}$ denotes the Green's tensor relating the electric current to electric field in the background configuration and $\chi_{\mathrm{e}}(\boldsymbol{r}) = \left(\varepsilon_{\mathrm{r}}(\boldsymbol{r}) - \varepsilon_{\mathrm{r}}^{\mathrm{b}}(\boldsymbol{r})\right)/\varepsilon_{\mathrm{r}}^{\mathrm{b}}(\boldsymbol{r})$ denotes the electric susceptibility of the total configuration, characterized by $\varepsilon_{\mathrm{r}}(\boldsymbol{r})$, with respect to the inhomogeneous background configuration, characterized by $\varepsilon_{\mathrm{r}}^{\mathrm{b}}(\boldsymbol{r})$. The Green's tensor $\overline{\overline{\boldsymbol{G}}}^{\mathrm{b}}$ represents the electric field radiated in the background configuration by an electric point source located in the pad domain $\mathcal{D}_{\mathrm{p}}$, which can be evaluated numerically as an off-line procedure. It should be noted that Equation [5] needs to be treated as an integral equation, which after

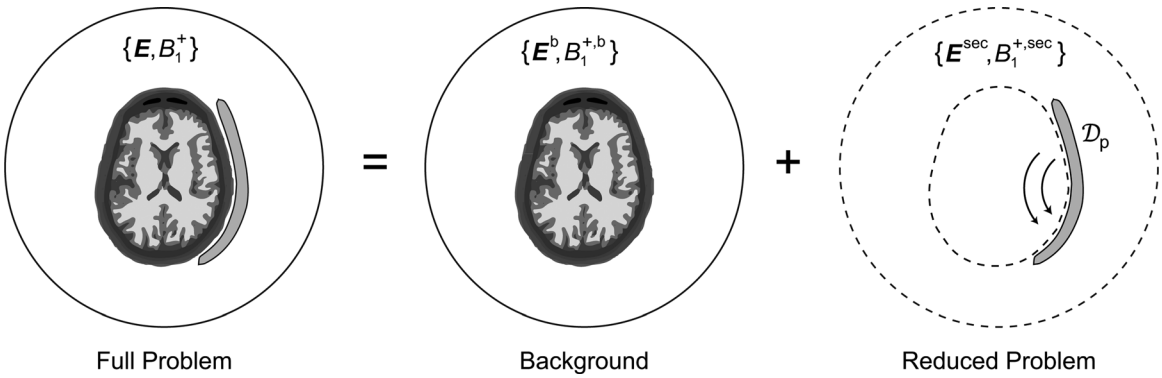

FIG. 1. Decomposition of a dielectric shimming configuration. The total field $\{\boldsymbol{E}, B_1^+\}$ (left) is decomposed into a primary field produced in the background configuration $\left\{\boldsymbol{E}^{\mathrm{b}}, B_1^{+,\mathrm{b}}\right\}$ (without pad; center) and a secondary field $\left\{\boldsymbol{E}^{\mathrm{sec}}, B_1^{+,\mathrm{sec}}\right\}$ (right) produced by the currents induced in the dielectric pad radiating in the background configuration. This splits the full problem into a stationary part, which can be evaluated off-line, and a reduced problem confined to the dielectric pad domain $\mathcal{D}_{\mathrm{p}}$.

discretization can be written as a system of linear equations and solved using iterative numerical methods. Obtaining a solution to Equation [5] for a given $\boldsymbol{E}^{\mathrm{b}}$ and χ_{e} is commonly referred to as the "forward problem."

Once the electrical interactions within the dielectric pad are solved for, the total B_1^+ field follows from the integral expression

$$B_1^+(\boldsymbol{r}) = B_1^{+,\mathrm{b}}(\boldsymbol{r}) + \int_{\boldsymbol{r}'\in\mathcal{D}_{\mathrm{p}}} \overline{\overline{\boldsymbol{G}}}^{+,\mathrm{b}}(\boldsymbol{r},\boldsymbol{r}')\chi_{\mathrm{e}}(\boldsymbol{r}')\boldsymbol{E}(\boldsymbol{r}')\mathrm{d}V, \quad [6]$$

in which $\overline{\overline{\boldsymbol{G}}}^{+,\mathrm{b}}$ denotes the Green's tensor relating the electric current to the B_1^+ field in the background configuration. This means that propagation of $B_1^{+,\mathrm{sec}}$ in the background configuration is accounted for via $\overline{\overline{\boldsymbol{G}}}^{+,\mathrm{b}}$. We note that, once the total electric field $\boldsymbol{E}$ is known, Equation [6] can be directly evaluated with the minor computational cost of evaluating the associated matrix-vector product.

Zero-Order Approximation

Approaches to solving Equation [5], and subsequently Equation [6], include the Neumann series expansion and the Born approximation (25). Previous studies have indicated that these methods can model moderate field perturbations but diverge for higher permittivities (24). In this study, we evaluated a modification of the Born approximation by neglecting the electrical interactions within the pad domain, which corresponds to the zero-order approximation as discussed in the Introduction. This amounts to setting $\boldsymbol{E} \approx \boldsymbol{E}^{\mathrm{b}}$ in Equation [6] as follows:

$$B_1^+(\boldsymbol{r}) \approx B_1^{+,\mathrm{b}}(\boldsymbol{r}) + \int_{\boldsymbol{r}'\in\mathcal{D}_{\mathrm{p}}} \overline{\overline{\boldsymbol{G}}}^{+,\mathrm{b}}(\boldsymbol{r},\boldsymbol{r}')\chi_{\mathrm{e}}(\boldsymbol{r}')\boldsymbol{E}^{\mathrm{b}}(\boldsymbol{r}')\mathrm{d}V \quad [7]$$

which is only strictly valid in the limit $\chi_{\mathrm{e}} \to 0$ but allows us to set apart the role of electrical interactions within the pad. We can also neglect the propagation in the background model by using the Green's tensor of free space, denoted by $\overline{\overline{\boldsymbol{G}}}_0^+$, for which an expression can be obtained using closed form analytical solutions (26). This is then written as

$$B_1^+(r) \approx B_1^{+,\mathrm{b}}(r) + \int_{\boldsymbol{r}'\in\mathcal{D}_{\mathrm{p}}} \overline{\overline{\boldsymbol{G}}}_0^+(\boldsymbol{r},\boldsymbol{r}')\chi_{\mathrm{e}}(\boldsymbol{r}')\boldsymbol{E}^{\mathrm{b}}(\boldsymbol{r}')\mathrm{d}V. \quad [8]$$

Inverse Problem Framework

In contrast to the forward problem in which a solution to the field is sought for a given pad, the inverse problem is posed in the opposite direction; for a given field, a solution is sought in terms of the dielectric pad. The method is formulated by minimizing a cost function that measures the difference between a desired B_1^+ field and the actual B_1^+ field, which is referred to as the "target field error," by iteratively updating the permittivity distribution in the pad domain $\mathcal{D}_{\mathrm{p}}$. This cost function F is formulated as

$$F = \|B_1^+ - B_1^{+,\mathrm{target}}\|^2_{\mathcal{D}_{\mathrm{ROI}}}, \quad [9]$$

where $\mathcal{D}_{\mathrm{ROI}}$ denotes the ROI (i.e., the spatial domain for which the target field is specified) and B_1^+ depends on the product of χ_{e} and $\boldsymbol{E}$ as given by Equation [6]. For fixed values of the electric field $\boldsymbol{E}$, this function is minimized by updating the permittivity distribution via χ_{e}. The electric field, however, changes in tandem with updated values of χ_{e} as shown in Equation [5], which means that its values need to be updated as well. The expressions involved in updating χ_{e} are given in the Appendix.

METHODS

3D B_1^+ Characterization Using FDTD

3D field simulations of a 7T neuroimaging setup were performed using a commercial software package (xFDTD 7.2, Remcom Inc., State College, Pennsylvania, USA). The transmit coil was modeled as a 16-rung high-pass birdcage (inner diameter 30 cm; rung length 18 cm) with unit voltage sources with an impedance of 50 Ω,

sinusoidal excitation at 300 MHz, and a 2π phase evolution along its circumference to simulate quadrature excitation in its homogeneous mode. The male body model "Duke" from the Virtual Family dataset was used (27).

A single dielectric pad was introduced on the left side of the head model with dielectric properties of either a calcium titanate ($CaTiO_3$) or a barium titanate ($BaTiO_3$) suspension. These suspensions have relative permittivity values of 110 and 286 and conductivity values of 0.11 S/m and 0.44 S/m, respectively, and have been used in previous neuroimaging studies at 7T (6–8,11). The dimensions of the pad were 18×18 cm with a thickness of 8 mm. All simulations were performed on a 4-mm isotropic grid.

2D Electromagnetic Modeling Using the Integral Equation Method

The integral equation method was implemented for a 2D TM-polarized configuration (electric field vector parallel to the invariance direction) of the neuroimaging setup with dielectric pad. A 2D approach was chosen to reduce the bookkeeping and computational complexity. This leads to an approximation of the fields that is reasonable in the central transverse plane of the coil (28), which is where the effects were analyzed. The inhomogeneous body model was incorporated into the background (hereinafter referred to as the "inhomogeneous background") as opposed to using a free space background. Interactions between the pad and the RF coil are assumed to be negligible (as described in more detail in the Discussion). The primary field (i.e., the field that is present in the background configuration without any pads in place) was generated by simulating a 30-cm-diameter circular array of 16 electric current line-sources, driven at a frequency of 300 MHz with a 2π phase evolution along its circumference, surrounding the transverse cross-section of the "Duke" head model (27). The Green's tensors were constructed by computing the field response of the inhomogeneous background for all source locations within the pad domain. All computations using the 2D method were performed on a 4-mm isotropic grid using the iterative conjugate gradient method (26). All customized software code was developed in MATLAB 8.0 (MathWorks, Natick, Massachusetts, USA) and run on a desktop computer: computations took less than 30 s, including all off-line procedures.

To illustrate the relevance of body propagation effects, the zero-order approximation was evaluated in the 2D configuration using either the Green's tensor of free space (Eq. [8]) or the Green's tensor of the inhomogeneous background (Eq. [7]) which accounts for the interactions with the body. In both cases, values for the electric field were taken from the primary field. As mentioned in the theory section, the zero-order approximation neglects electrical interactions within the dielectric pad; the relevance of these interactions is illustrated by comparison with full-wave results (Eq. [6]).

Development of a 2D Inverse Design Method

The full-wave 2D integral equation method with inhomogeneous background was used to develop an inversion method in which the algorithm optimizes the design of a dielectric pad by iteratively updating the permittivity within the pad domain through the real part of χ_e via minimization of the target field error. Mathematical details on the update procedure are outlined in the Appendix. To avoid spurious results, we applied a positivity constraint by enforcing negative values of χ_e to zero after each update.

As a proof-of-concept, we evaluated the inversion method both with the free-space as well as the inhomogeneous background for a synthetic target field dataset. The target field was generated by simulating the 2D configuration with a lossless barium titanate pad of homogeneous permittivity ($\varepsilon_r = 286$). The resulting B_1^+ data in the body was then provided to the algorithm as a target field in complex form (i.e., magnitude and phase). The pad geometry was assumed to be known in advance, and the reconstructed permittivity was allowed to vary within this domain. The accuracy of the reconstruction result was evaluated by measuring the global error in the reconstructed permittivity as follows:

$$\mathrm{ERR}_\varepsilon = \frac{\|\varepsilon - \varepsilon^{\mathrm{true}}\|_{\mathcal{D}_p}}{\|\varepsilon^{\mathrm{true}}\|_{\mathcal{D}_p}}. \quad [10]$$

Experimental validation of the 2D inverse design method was performed in a cylindrical phantom. The phantom was 12 cm in diameter and 24 cm in length and had a measured relative permittivity of 78 and electrical conductivity of 0.9 S/m. The inversion method was set up to aim for a uniform B_1^+ magnitude of 1 μT, which is equal to the peak magnitude of the primary B_1^+ field, within a manually drawn ROI. The algorithm was adapted to handle the target B_1^+ field in magnitude form by transferring the B_1^+ phase of the previous iteration to the target field, which is a common procedure in RF shimming and RF pulse design (29). Furthermore, the pad domain was defined as a layer of 6-mm thickness surrounding the phantom, in which the permittivity was allowed to vary. Because an inhomogeneous permittivity distribution is currently challenging to implement, a simplified version of the resulting profile was implemented using a homogeneous barium titanate suspension ($\varepsilon_r = 286$) to form a rectangular pad with a length equal to that of the phantom. The required width and position were determined by measuring the extent across which the optimized permittivity distribution was higher than a relative permittivity of 200. Although this approach is somewhat ad hoc, it allows for comparing simulated and experimental data. B_1^+ maps were acquired using the dual refocused echo acquisition mode sequence (30). The spatial resolution was $2.5 \times 2.5 \times 5.0$ mm^3, the B_1^+ encoding tip angle 50° and the imaging tip angle 10°.

RESULTS

3D B_1^+ Characterization

Figure 2 shows the simulated (xFDTD) B_1^+ field distributions in a transverse cross-section through the head. The calcium titanate pad gives rise to a uniform increase of the B_1^+ in the vicinity of the pad, which is consistent with the zero-order formulation. On the other hand, the barium titanate pad, which has a much higher

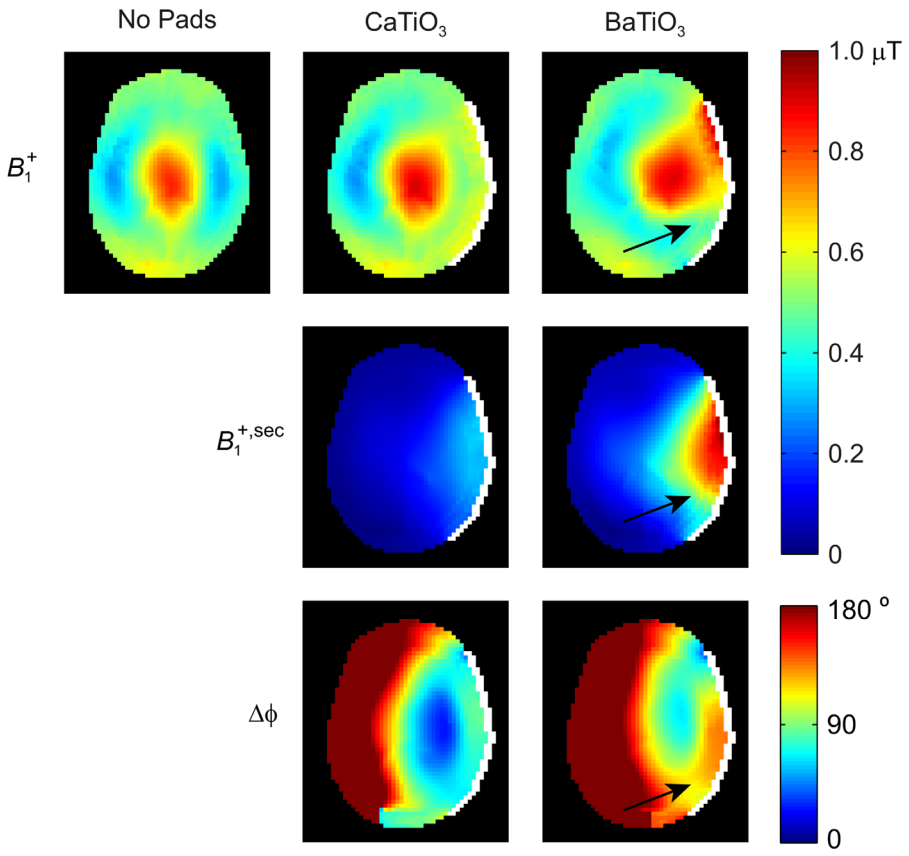

FIG. 2. Effect of two different dielectric pads on the B_1^+ field. Shown are the 3D simulated transverse cross-sections of the total B_1^+ field (top) and the secondary B_1^+ field in magnitude (middle) and relative phase (bottom). The calcium titanate ($CaTiO_3$) pad induces a uniform increase of the B_1^+ close to the pad. Moving to barium titanate ($BaTiO_3$) introduces a strong anterior/posterior asymmetry in the total B_1^+ field (arrows), which is related to both the magnitude as well as the relative phase of the secondary B_1^+ field. The dielectric pads are shown in white.

permittivity, leads to a much stronger but also asymmetric B_1^+ distribution in the anterior/posterior direction. This behavior clearly does not follow the zero-order formulation, which would suggest constructive B_1^+ elevation along the entire extent of the pad. From the magnitude of the secondary field, which is obtained as a complex subtraction of the primary B_1^+ field (without pad) from the total B_1^+ field with the dielectric pad, it can be seen that the calcium titanate pad introduces an evenly distributed secondary field. In addition, the phase difference with respect to the primary B_1^+ field is relatively small ($<70°$) and, more importantly, rather uniform along the extent of the dielectric. This explains the uniform B_1^+ elevation in the vicinity of the pad. In contrast, the barium titanate pad introduces a secondary B_1^+ field that is asymmetric in magnitude but also features an asymmetric and larger phase difference with respect to the primary B_1^+ field, reaching almost 160° on the posterior side of the brain. Both terms account for the resulting anterior/posterior asymmetry observed in the total B_1^+ field distribution, with constructive interference on the anterior side and destructive interference at the posterior side.

Figure 3 illustrates the magnitude of the induced current density $\boldsymbol{J}_i$ in the transverse plane for the three configurations. As can be seen, the induced current density in the barium titanate pad is much stronger than in the calcium titanate pad. Furthermore, the calcium titanate pad supports a rather uniform current density, whereas the induced current density in the barium titanate pad is highly nonuniform. The asymmetric B_1^+ induced by the barium titanate pad also corresponds to the asymmetric induced current density with a strong intensity in the anterior part of the pad.

2D Electromagnetic Analysis Using the Integral Equation Method

The 2D simulation results using the integral equation method are shown in Figure 4, showing the secondary B_1^+ field for different levels of model complexity. The zero-order approximation, which does not account for electrical interactions within the pad, is shown both for the Green's tensor of free-space (Eq. [8]) as well as the Green's tensor of the inhomogeneous background, which accounts for the body model (Eq. [7]). Clearly, using the Green's tensor of free-space does not yield an accurate representation of the physical case but shows that the spatial structure of the secondary field is governed by the background model, with an increased magnitude close to the pad, and a decreased magnitude at further distance. This is evident since the body is close to the pad, and presents a substantial load to the secondary field. Finally, the full-wave solution (Eq. [6]) shows the relevance of electrical interactions within the dielectric pad. In the calcium titanate pad, the zero-order approximation with inhomogeneous background was relatively accurate with deviations in the order of ~10% in the corresponding total B_1^+ field (data not shown). In the barium titanate pad, however, the accuracy was insufficient and only the full-wave method captured the asymmetric magnitude profile as also shown in Figure 2. The added

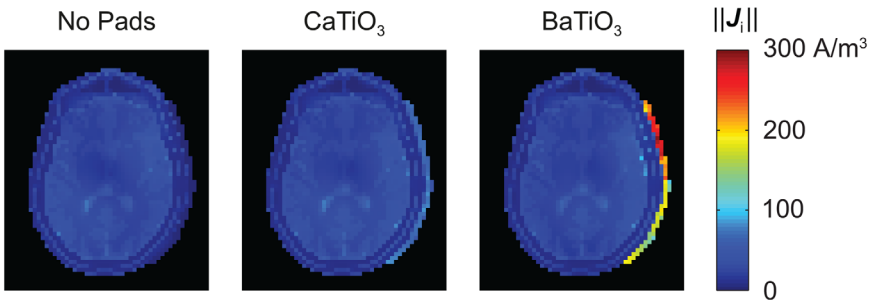

FIG. 3. Magnitude of the induced current density $\boldsymbol{J}_i$ in the transverse plane, evaluated in the 3D configuration. The calcium titanate ($CaTiO_3$) pad supports a rather uniform induced current density, while the induced current density in the barium titanate ($BaTiO_3$) pad features a strong anterior/posterior asymmetry.

benefit of using the inhomogeneous background in this case was observed in the convergence rate of the solver, which was improved approximately fivefold compared with the conventional 2D full-wave method based on a free-space background.

2D Inverse Design Method

Figure 5 shows the proof-of-concept inversion results using either the free space or the inhomogeneous background model. When using the free space background, the inversion method converged to the target field albeit with substantial errors in the reconstructed permittivity, which is reflected in a global permittivity error (Eq. [10]) of $ERR_\varepsilon = 12.5\%$. The accuracy of the reconstructed permittivity is much improved in the method based on the inhomogeneous background, with a global error of $ERR_\varepsilon = 3.9\%$. The convergence of both inversion methods (Eq. [9]) is shown in Figure 6, which also reflects a much improved convergence rate of the latter method.

Figure 7 shows the inverse design results, in which the inversion method with inhomogeneous background was used together with the phase-updating scheme. The target field was defined as a uniform B_1^+ magnitude of 1 μT within a manually drawn ROI and the pad domain was defined as a continuous layer around the cylindrical phantom. Convergence was obtained within five iterations. The optimized dielectric was implemented as a homogeneous pad as shown in Figure 8. The results indicate that the B_1^+ field can be tailored to an arbitrary ROI using the inversion method. Qualitative agreement with experimental B_1^+ maps demonstrates the validity of the method.

DISCUSSION

In this study, the effects of high permittivity materials on the RF field were analyzed using concepts from electromagnetic scattering. Whereas a calcium titanate pad gave a consistent elevation of the B_1^+ in its vicinity, a barium titanate pad with higher permittivity led to areas of high as well as low B_1^+ close to the pad. This effect can be attributed to the interference of a secondary magnetic field that is produced in the body by the currents induced in the dielectric pad, as embodied in the integral equation method with an inhomogeneous background. A full-wave model based on this formulation provides an efficient method for modeling these effects and improves the convergence of the inversion method substantially. This framework provides a promising starting point for tailored design of dielectric pads.

The scattering formalism applied here to dielectric shimming provides fundamental insight into the physical interactions that take place when a dielectric pad is inserted. Equation [6] states that a dielectric pad can be seen as a collection of equivalent currents, which radiate a secondary field into the background configuration. The expression indicates that, for a given electric field, the

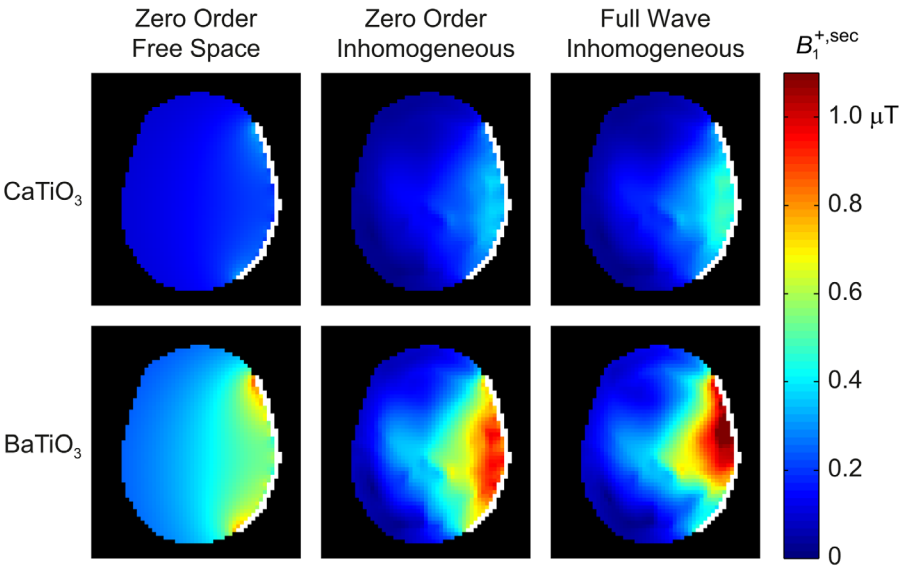

FIG. 4. Approximations of the secondary B_1^+ field evaluated in the 2D configuration using the integral equation method. The zero-order approximation using either the free space (Eq. 8) or inhomogeneous background model (Eq. 7) shows the necessity of including body propagation effects. The full-wave method (Eq. 6) illustrates the relevance of electrical interactions within the pad, which become significant as the permittivity of the pad increases.

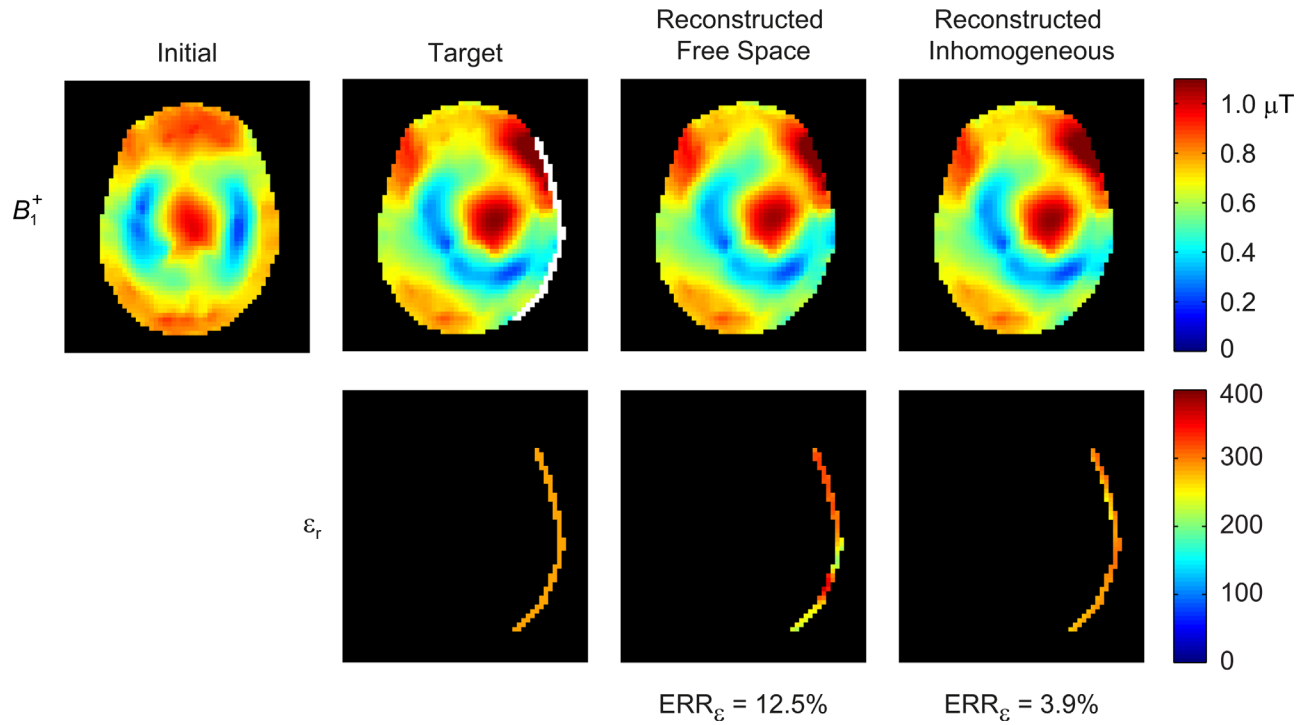

FIG. 5. Proof-of-concept reconstruction results of the inversion method based on the free space or inhomogeneous background. The agreement between the reconstructed and true permittivity is much improved by using the inhomogeneous background, reducing the global permittivity error (Eq. 10) from $ERR_\varepsilon = 12.5\%$ down to $ERR_\varepsilon = 3.9\%$.

magnitude of the secondary B_1^+ field is related to both the permittivity as well as the volume of the pad. This relationship has been exploited previously to reduce the thickness of the dielectric pad by using materials with a higher permittivity (2,8) or by tailoring the geometry of the pad for a given permittivity (3,9). However, a quantitative description of the effects cannot be based solely on Equation [6] and requires the electric field to be solved based on Equation [5]. This is further illustrated using the zero-order approximation, which was shown to be reasonably accurate for low levels of electrical interactions, such as with the calcium titanate pad, but does not account for potential wavelength effects within the pad, as was the case in the higher permittivity pad made of barium titanate. Only the full-wave method could model such effects accurately. This dependence can also be related to the dimensions of the pad with respect to the RF wavelength in the high permittivity material: in the calcium titanate pad, this is about 9.5 cm, whereas for the barium titanate pad it is 5.8 cm. In other words, a calcium titanate pad would also exhibit similar wavelength effects if a much larger pad size were to be considered.

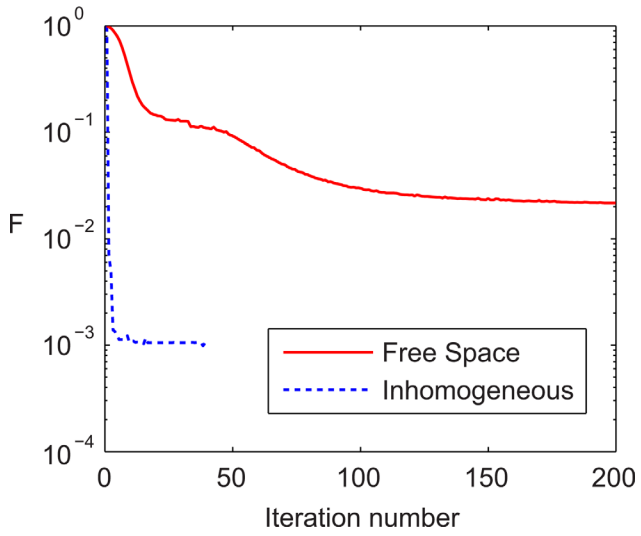

FIG. 6. Convergence of the target field error in the proof-of-concept inversion experiment. By using the inhomogeneous background model, the inversion method requires many fewer iterations and reaches a lower target field error (Eq. 9).

The full-wave method based on the integral equations with inhomogeneous background simplifies the forward problem of computing the fields substantially, since the problem is reduced to resolving only the unknown electrical interactions within the dielectric pad itself, by accounting for all other interactions in an off-line stage. This was found to improve the convergence rate approximately fivefold in the 2D method and is expected to provide even greater improvements in a 3D method, since the relative size of the pad domain is then even smaller. An additional benefit of the approach is that the electric field strength within the heterogeneous body model is available at no additional computational cost. This improves the relevance of the method when compared with analytical methods, which do not allow for realistic evaluation of local SAR because they do not support a heterogeneous body model (31).

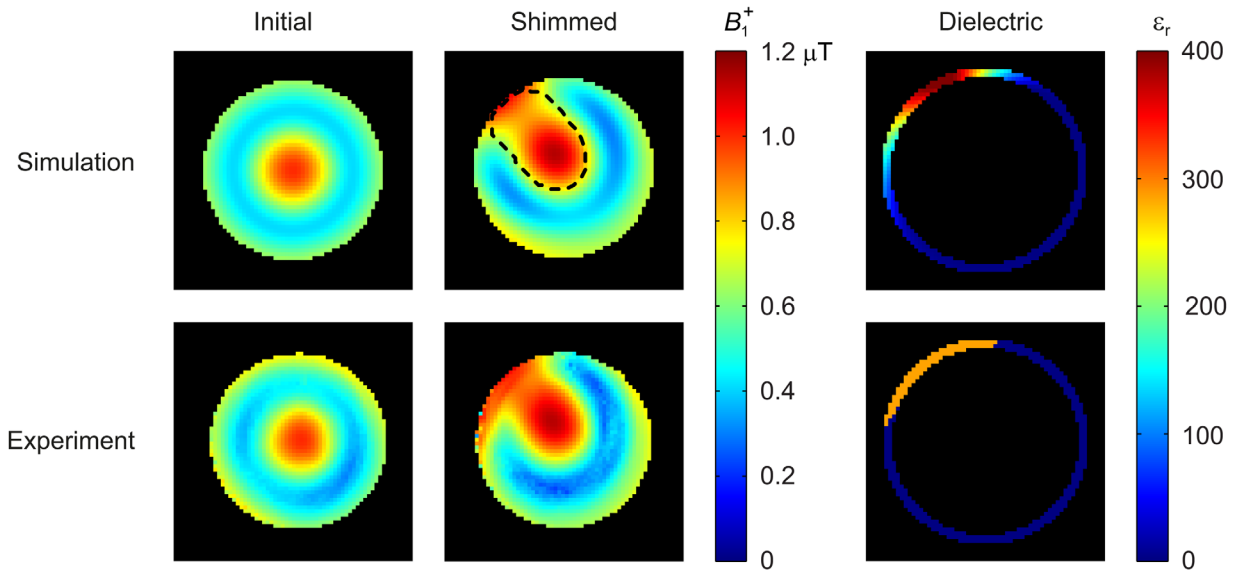

FIG. 7. Experimental validation of the 2D Inverse design method in a cylindrical phantom. The method aims at obtaining a uniform B_1^+ magnitude of 1 μT within a manually drawn ROI (dashed line), by optimizing the permittivity distribution within a continuous layer surrounding the phantom. The optimized permittivity distribution was implemented as a homogeneous pad using barium titanate ($\varepsilon_r = 286$), its dimensions were obtained by truncating the optimized profile at $\varepsilon_r = 200$. Agreement with experimental B_1^+ maps demonstrates the validity of the method.

In addition to reducing the complexity of the forward problem, introducing the inhomogeneous background also reduces the ill-posedness of the associated inverse problem and provides additional insight into the nature of this optimization problem. Equation [6] indicates that designing dielectric pads can be thought of as designing an induced current density within the pad domain such that a desired secondary B_1^+ field is generated. These induced currents, however, are the result of passive electrical interactions within the pad and within the inhomogeneous background, which need to satisfy Maxwell's equations through Equation [5]. The proposed method reduces the complexity of both steps significantly, since the field decomposition (e.g., Eqs. [4] and [6]) provides a direct relationship between the secondary B_1^+ field in the body and the induced currents in the pad domain. Furthermore, because updates of the induced current density are explicitly limited to the pad domain, the effective number of unknowns associated with the inverse problem is reduced significantly, thereby reducing its ill-posedness. The framework also indicates that the optimization problem is nonlinear in the sense that the electric field $\boldsymbol{E}$ and susceptibility χ_e are both unknown and occur as a product in Equation [6]. This nonlinearity is illustrated in Figure 5, where both algorithms converge to the target field even though not fully reconstructing the actual permittivity, reflecting the presence of local minima in the solution space. It is interesting to note that this property is fundamentally different from RF shimming using multiple independent sources (i.e., a transmit array), because in that case superposition can be applied, representing in principle a linear optimization problem.

In the current implementation of the proposed integral equation method, interactions between the dielectric pad and the RF coil have been neglected (i.e., the inhomogeneous background did not include the RF coil). This means that the Green's tensor only accounts for interactions between the dielectric pad and the body, which is reasonable when the body dominates these coupling effects, for instance in volume coils where the dielectric pad is close to the body and relatively small with respect to the size of the RF coil. This simplification could, however, pose limitations when the size or permittivity of the dielectric pad increases, or when it is positioned closer to the coils' conductors (14,17). In such a case, coupling between the dielectric pad and the coil may become significant, which means that the coil would need to be included in the background model in order to account for these effects. We note that in a practical setting, the coil would also be retuned, which effectively compensates for some of these interactions. Other limitations include the 2D approximation of the RF field. This approximation works well for longitudinal configurations, as shown in Figure 7, but loses accuracy when considering for instance a dielectric pad with an axial extent that is short with respect to the RF coil. The method, however, can potentially be extended to 3D configurations in a similar manner, although requiring significant development due to the vectorial nature of the related integral equation (26). Furthermore, in the inversion method, the permittivity was allowed to vary within the pad domain, which increases the degrees of freedom and flexibility of the algorithm but results in an inhomogeneous permittivity distribution that is more difficult to implement. In the current study, the optimized permittivity distribution was implemented by constructing a homogeneous pad instead; its geometry and position were set to match the area in which the optimized relative permittivity was 200 or higher. This is a very simple approach that is sufficient for the purpose of

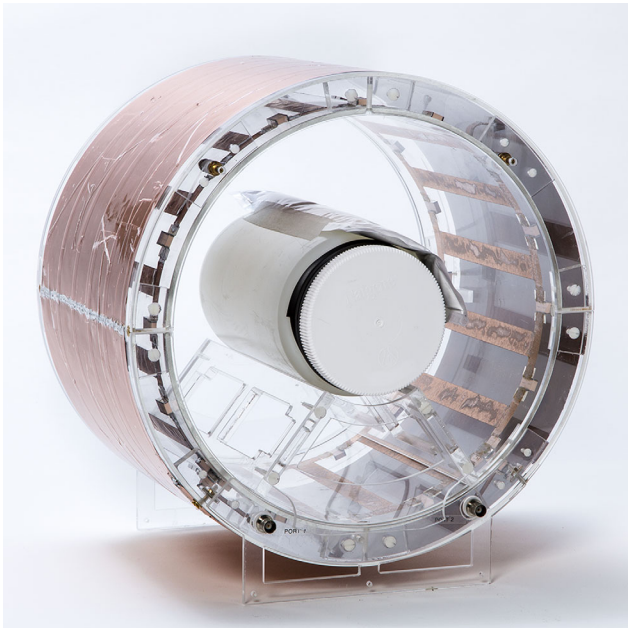

FIG. 8. Experimental setup used to evaluate the 2D inversion method. The dielectric pad (shown in Fig. 7) is positioned on top of the cylindrical phantom.

experimental validation, but the procedure can also be integrated in the algorithm by incorporating appropriate constraints on the permittivity (32,33).

Finally, we note that the proposed framework is applicable to all field strengths and all dielectric shimming configurations. The method allows for incorporating a realistic body model and can account for dielectric pads of arbitrary shape and composition. This paves the way for exploiting the possibilities of dielectric shimming for addressing B_1^+ inhomogeneity in high field MRI.

APPENDIX A: UPDATING THE ELECTRIC SUSCEPTIBILITY χ_e

The update process of χ_e aims to iteratively minimize the target field error, which is measured through the cost function as given by Equation [9], repeated here for convenience:

$$F_n(\chi_{e,n}) = \|\rho_n \chi_{e,n}\|^2_{\mathcal{D}_{ROI}}. \qquad [A1]$$

Here, $\rho_n(\chi_{e,n}) = B_1^+(\chi_{e,n}) - B_1^{+,target}$ denotes the target field error and $\chi_{e,n}$ denotes the electric susceptibility at iteration n. The target field error is minimized by sequentially updating the electric susceptibility $\chi_{e,n}$ and updating the corresponding electric field $\boldsymbol{E}$ by solving a forward problem. The updates for $\chi_{e,n}$ are formulated using a gradient descend approach by defining a sequence of updates in χ_e as

$$\chi_{e,n} = \chi_{e,n-1} + \beta_n \nabla F_n, \qquad [A2]$$

where ∇F_n denotes the gradient of the cost function with respect to χ_e, as follows:

$$\nabla F_n(r) = \overline{\boldsymbol{E}(\boldsymbol{r})} \int_{r' \in \mathcal{D}_p} \overline{\overline{\boldsymbol{G}}^{+,b}(\boldsymbol{r},\boldsymbol{r}')} \rho_{n-1}(\boldsymbol{r}') dV, \qquad [A3]$$

where the overbar denotes a complex conjugate and the scalar step size β_n is obtained using line-minimization.

REFERENCES

1. Yang QX, Wang J, Wang J, Collins CM, Wang C, Smith MB. Reducing SAR and enhancing cerebral signal-to-noise ratio with high permittivity padding at 3 T. Magn Reson Med 2011;65:358–362.
2. De Heer P, Brink WM, Kooij BJ, Webb AG. Increasing signal homogeneity and image quality in abdominal imaging at 3 T with very high permittivity materials. Magn Reson Med 2012;68:1317–1324.
3. Brink WM, Webb AG. High permittivity pads reduce specific absorption rate, improve B1 homogeneity, and increase contrast-to-noise ratio for functional cardiac MRI at 3 T. Magn Reson Med 2014;71:1632–1640.
4. Yang QX, Rupprecht S, Luo W, et al. Radiofrequency field enhancement with high dielectric constant (HDC) pads in a receive array coil at 3.0T. J Magn Reson Imaging 2013;38:435–440.
5. Lindley MD, Kim D, Morrell G, Heilbrun ME, Storey P, Hanrahan CJ, Lee VS. High-permittivity thin dielectric padding improves fresh blood imaging of femoral arteries at 3 T. Invest Radiol 2015;50:101–107.
6. Snaar JEM, Teeuwisse WM, Versluis MJ, van Buchem MA, Kan HE, Smith NB, Webb AG. Improvements in high-field localized MRS of the medial temporal lobe in humans using new deformable high-dielectric materials. NMR Biomed 2011;24:873–879.
7. Teeuwisse WM, Brink WM, Webb AG. Quantitative assessment of the effects of high-permittivity pads in 7 Tesla MRI of the brain. Magn Reson Med 2012;67:1285–1293.
8. Teeuwisse WM, Brink WM, Haines KN, Webb AG. Simulations of high permittivity materials for 7 T neuroimaging and evaluation of a new barium titanate-based dielectric. Magn Reson Med 2012;67:912–918.
9. Brink WM, van der Jagt AMA, Versluis MJ, Verbist BM, Webb AG. High permittivity dielectric pads improve high spatial resolution magnetic resonance imaging of the inner ear at 7 T. Invest Radiol 2014;49:271–277.
10. Luo W, Lanagan MT, Sica CT, Ryu Y, Oh S, Ketterman M, Yang QX, Collins CM. Permittivity and performance of dielectric pads with sintered ceramic beads in MRI: early experiments and simulations at 3 T. Magn Reson Med 2013;70:269–275.
11. O'Brien KR, Magill AW, Delacoste J, Marques JP, Kober T, Fautz H-P, Lazeyras F, Krueger G. Dielectric pads and low- B1+ adiabatic pulses: complementary techniques to optimize structural T1 w whole-brain MP2RAGE scans at 7 Tesla. J Magn Reson Imaging 2014;40:804–812.
12. Yang QX, Mao W, Wang J, Smith MB, Lei H, Zhang X, Ugurbil K, Chen W. Manipulation of image intensity distribution at 7.0 T: passive RF shimming and focusing with dielectric materials. J Magn Reson Imaging 2006;24:197–202.
13. Rupprecht S, Sica CT, Sahul R, Kwon S, Lanagan MT, Yang QX. Drastic Enhancement and Manipulation of RF Field with Ultra High Dielectric Constant (uHDC) Material at 3T. In: Proceedings of the 21st Annual Meeting of ISMRM, Salt Lake City, Utah, USA, 2013. p. 396.
14. Oh S, Luo W, Zhang B, Deniz CM, Lanagan MT, Wiggins GC, Collins CM. Maximized Local B1+ using Optimized Dielectric Pad at 7 T: Numerical Optimization and Experimental Validation. In: Proceedings of the 21st Annual Meeting of ISMRM, Salt Lake City, Utah, USA, 2013. p. 4381.
15. Jayatilake ML, Storrs J, Chu W-J, Lee J-H. Theoretical determination of the dielectric constant for passive RF shimming at high field. In: Proceedings of the 19th Annual Meeting of ISMRM, Montreal, Canada, 2011. p. 3887.
16. Ketterman MD, Yang QX, Webb AG, Herse Z, Neuberger T, Carluccio G, Lanagan MT. MRI Signal Enhancement via High-Permittivity Material Pads. In: Proceedings of the 21st Annual Meeting of ISMRM, Melbourne, Victoria, Australia, 2012. p. 2699.
17. Carluccio G, Oh S, Yang QX, Erricolo D, Luo W, Collins CM. Near-Field Wave Impedance Matching with High-Permittivity Dielectric

Materials for Optimum Transmittance in MRI Systems. In: Proceedings of the 21st Annual Meeting of ISMRM, Salt Lake City, Utah, USA, 2013. p. 4374.
18. Winkler SA, Sbrizzi A, van den Berg CAT, Luijten PR, Rutt BK. Optimized Dielectric Shimming in High-Field Magnetic Resonance Imaging: A Theoretical Approach. In: Proceedings of the Workshop Scattering by Aggregates, Bremen, Germany, 2014. p. 70–73.
19. Lattanzi R, Vaidya MV, Carluccio G, Sodickson DK, Collins CM. Effects of High-Permittivity Materials on Absolute RF Coil Performance as a Function of B0 and Object Size. In: Proceedings of the 22nd Annual Meeting of ISMRM, Milan, Italy, 2014. p. 4818.
20. Lattanzi R, Vaidya M V, Carluccio G, Sodickson DK, Collins CM. Signal-to-Noise Ratio Gain at 3T Using a Thin Layer of High-Permittivity Material Inside Enclosing Receive Arrays. In: Proceedings of the 22nd Annual Meeting of ISMRM, Milan, Italy, 2014. p. 4814.
21. Abubakar A, Hu W, van den Berg PM, Habashy TM. A finite-difference contrast source inversion method. Inverse Probl 2008;24: 065004.
22. Endo M, Čuma M, Zhdanov MS. A multigrid integral equation method for large-scale models with inhomogeneous backgrounds. J Geophys Eng 2008;5:438–447.
23. Chen X. Subspace-based optimization method for inverse scattering problems with an inhomogeneous background medium. Inverse Probl 2010;26:074007.
24. Brink WM, Webb AG. A Forward Model Analysis of Dielectric Shimming in Magnetic Resonance Imaging. In: Proceedings of the 15th Annual Meeting of ICEAA, Torino, Italy, 2013. pp. 528–531.
25. Newton RG. Scattering theory of waves and particles. 2nd ed. Mineola, NY: Dover Publications; 2013.
26. Zwamborn P, van den Berg PM. The three-dimensional weak form of the conjugate gradient FFT method for solving scattering problems. IEEE Trans Microw Theory Tech 1992;40:1757–1766.
27. Christ A, Kainz W, Hahn EG, et al. The Virtual Family—development of surface-based anatomical models of two adults and two children for dosimetric simulations. Phys Med Biol 2010;55:N23–N38.
28. Van den Bergen B, Stolk CC, van den Berg JB, Lagendijk JJW, van den Berg CAT. Ultra fast electromagnetic field computations for RF multi-transmit techniques in high field MRI. Phys Med Biol 2009;54: 1253–1264.
29. Setsompop K, Wald LL, Alagappan V, Gagoski BA, Adalsteinsson E. Magnitude least squares optimization for parallel radio frequency excitation design demonstrated at 7 Tesla with eight channels. Magn Reson Med 2008;59:908–915.
30. Nehrke K, Versluis MJ, Webb A, Börnert P. Volumetric B(1) (+) Mapping of the Brain at 7T using DREAM. Magn Reson Med 2014;71:246–256.
31. Collins CM, Li S, Smith MB. SAR and B1 field distributions in a heterogeneous human head model within a birdcage coil. Magn Reson Med 1998;40:847–856.
32. Crocco L, Isernia T. Inverse scattering with real data: detecting and imaging homogeneous dielectric objects. Inverse Probl 2001;17:1573–1583.
33. Abubakar A, van den Berg PM. The contrast source inversion method for location and shape reconstructions. Inverse Probl 2002;18:495–510.